land

MDPI

Article

Monitoring of Glacier Area Changes in the Ili River Basin during 1992–2020 Based on Google Earth Engine

Qinqin Zhang [1,2,3,4,5], Zihui Zhang [1,2,3,4], Xiaofei Wang [1,2,3,4], Zhonglin Xu [1,2,3,4,*] and Yao Wang [1,2,3,4,6,*]

1 College of Ecology and Environment, Xinjiang University, Urumqi 830017, China; haozqqhao@stu.xju.edu.cn (Q.Z.); 18899595195@163.com (Z.Z.); 107552101154@stu.xju.edu.cn (X.W.)
2 Key Laboratory of Oasis Ecology, Xinjiang University, Urumqi 830017, China
3 Xinjiang Jinghe Observation and Research Station of Temperate Desert Ecosystem, Ministry of Education, Urumqi 830017, China
4 Technology Innovation Center for Ecological Monitoring and Restoration of Desert-Oasis, Ministry of Natural Resource, Urumqi 830001, China
5 Xinjiang Academy of Surveying and Mapping, Urumqi 830002, China
6 Institute of Desert Meteorology, China Meteorological Administration, Urumqi 830002, China
* Correspondence: zlxu@xju.edu.cn (Z.X.); wangyao@idm.cn (Y.W.)

Abstract: The Ili River Basin, a crucial transboundary river in the arid region of Central Asia, plays a significant role in the region's ecology and water resources. However, current methods for monitoring glacier area changes in this region face challenges in automation and accuracy due to the complex terrain and climatic conditions. This study aims to evaluate the effectiveness of the Google Earth Engine (GEE) platform for monitoring glacier area changes in the Ili River Basin from 1992 to 2020, with a focus on improving data accuracy and processing efficiency. Utilizing the Landsat data series, we employed the random forest (RF) classification algorithm within the GEE platform to extract glacier areas, optimizing a multidimensional feature set using the Jeffries–Matusita (JM) distance method, and applied visual interpretation for data refinement. Our results demonstrated that the GEE platform, combined with the RF algorithm, provided high accuracy in glacier monitoring, achieving an overall accuracy of 89% and a kappa coefficient of 0.85. During the study period, the glacier area in the Ili River Basin decreased by 184.76 km^2, with an average annual retreat rate of 6.84 km^2, most notably between 3800 and 4400 m in elevation. The analysis revealed that temperature changes had a more pronounced impact on glacier dynamics than precipitation. This approach significantly enhances image utilization efficiency and data processing speed, offering a reliable tool for monitoring glacier dynamics. Future research should focus on integrating additional environmental variables and extending the temporal scope to further refine glacier dynamics modeling and predictions.

Keywords: Google Earth Engine; glacier area; Ili River Basin; random forest algorithm; feature optimization

check for updates

Citation: Zhang, Q.; Zhang, Z.; Wang, X.; Xu, Z.; Wang, Y. Monitoring of Glacier Area Changes in the Ili River Basin during 1992–2020 Based on Google Earth Engine. *Land* **2024**, *13*, 1417. https://doi.org/10.3390/land13091417

Academic Editor: Xiangzheng Deng

Received: 30 July 2024
Revised: 30 August 2024
Accepted: 30 August 2024
Published: 3 September 2024

Copyright: © 2024 by the authors. Licensee MDPI, Basel, Switzerland. This article is an open access article distributed under the terms and conditions of the Creative Commons Attribution (CC BY) license (https://creativecommons.org/licenses/by/4.0/).

1. Introduction

Glaciers are represented as a critical freshwater resource with undeniable importance in arid areas, particularly in the arid zones of Central Asia [1]. The arid region of northwestern China is considered a key component of Asia's arid zones, where more than one-third of the surface runoff is derived from glacier melt, meaning that glacier and snow meltwater serve as a substantial water source in the region [2,3]. The accumulation and melting of glaciers in the upper reaches of these inland waters are profoundly affected by climate change, making them sensitive indicators of climate change [4,5]. In recent years, glacier melt in arid regions around the world has intensified due to the increasing frequency and severity of extreme heat and drought events, driven by climate change. These conditions accelerate the loss of glacial mass, leading to the widespread retreat of glaciers. This retreat

not only diminishes vital freshwater resources but also disrupts local ecosystems, exacerbates water scarcity issues, and poses significant challenges to communities that depend on glacial meltwater for agriculture, hydropower, and drinking water. The compounding effects of these extreme climatic events are creating a feedback loop that further accelerates glacier degradation, threatening the stability of water supplies in many vulnerable regions [6–8].

With this in mind, monitoring the variation in glaciers is fundamental for sustainable development of these regions. Currently, several methods are employed to monitor the variation in glaciers. Remote-sensing technology, such as satellite imagery and aerial photography, is widely utilized due to its efficiency in covering large and inaccessible areas [9,10]. This method enables the continuous observation of glacier size, volume, and movement over time. Ground-based observations, including the use of GPS and traditional surveying techniques, provide highly accurate data on glacier changes but are restricted to accessible regions [11]. Additionally, geodetic methods, involving the measurement of changes in the Earth's shape, gravity field, and rotation, offer insights into the mass balance of glaciers [12,13]. These methods are capable of detecting subtle changes in glacier mass and providing valuable data for understanding glacier dynamics.

Over the past decade, innovative solutions for the analysis and visualization of geospatial data have been provided by the emergence of cloud computing platforms. Among these, the Google Earth Engine (GEE) is renowned as a global leader in petabyte-level geographic data science analysis and visualization [14]. The traditional methods for data acquisition, preprocessing, information extraction, analysis, and application found in conventional remote-sensing software have been transformed by GEE [15,16]. By utilizing JavaScript and Python for programming, the GEE platform offers rapid and unrestricted batch data processing, substantially aiding remote-sensing scientists in conducting wide-ranging studies in fields such as land-use change [17], water resource monitoring [18], ecological environment quality evaluation [19,20], and agricultural monitoring [21,22]. In addition, with the help of machine learning technology, such as random forests (RFs), Support Vector Machines (SVMs), Generative Adversarial Networks (GANs), Hidden Markov Models (HMMs), etc., the GEE platform has further enhanced the ability to analyze complex geospatial patterns and predict future trends.

In this study, the variation in glaciers in the Ili River basin (relatively richer in water resources in the arid region of northwest China compared with other areas) was investigated using the GEE cloud platform. Multisource remote-sensing data, topographical data, and the RF algorithm were combined in this analysis. We aimed to (1) evaluate the suitability of the constructed feature set (including attributes such as optics, texture, and topography) in discerning glacier and non-glacier in our study area; and (2) investigate the variation in the glaciers in the study area during 1992–2020. The corresponding research would offer a new pathway for the rapid and precise acquisition of glacier changes, thereby revitalizing glacier research in arid regions.

2. Materials and Methods

2.1. Study Area

The Ili River Basin, a part of the Central Asian inland river system, is internationally shared between China and Kazakhstan. It is recognized as the region with the most abundant water resources in China's Tianshan Mountains, containing many of the rivers in Xinjiang with the highest runoff volumes (Figure 1). Within China, the Ili River Basin (41°14′–44°51′ N, 80°15′–86°56′ E) spans an area of 5.76×10^4 km^2, accounting for 38% of the total basin area. Across the entire basin, the mean annual temperature ranges from 2.9 to 9.1 °C. In the valleys, the annual precipitation is approximately 300 mm, whereas in mountainous regions, it ranges from 500 to 1000 mm. This region is known as the wet island among the arid zones of Xinjiang and Central Asia [23]. Modern glaciers are prevalent across the mountainous areas of the Ili River Basin, exhibiting snow lines that vary from 3630 to 3840 m, with an average elevation of 3730 m. The meltwater resources of these

glaciers are substantial and regulate the river flow [24,25]. Amidst the current backdrop of global warming, the glacier areas in the Ili River Basin have experienced considerable transformations, exhibiting a retreating trend overall [26].

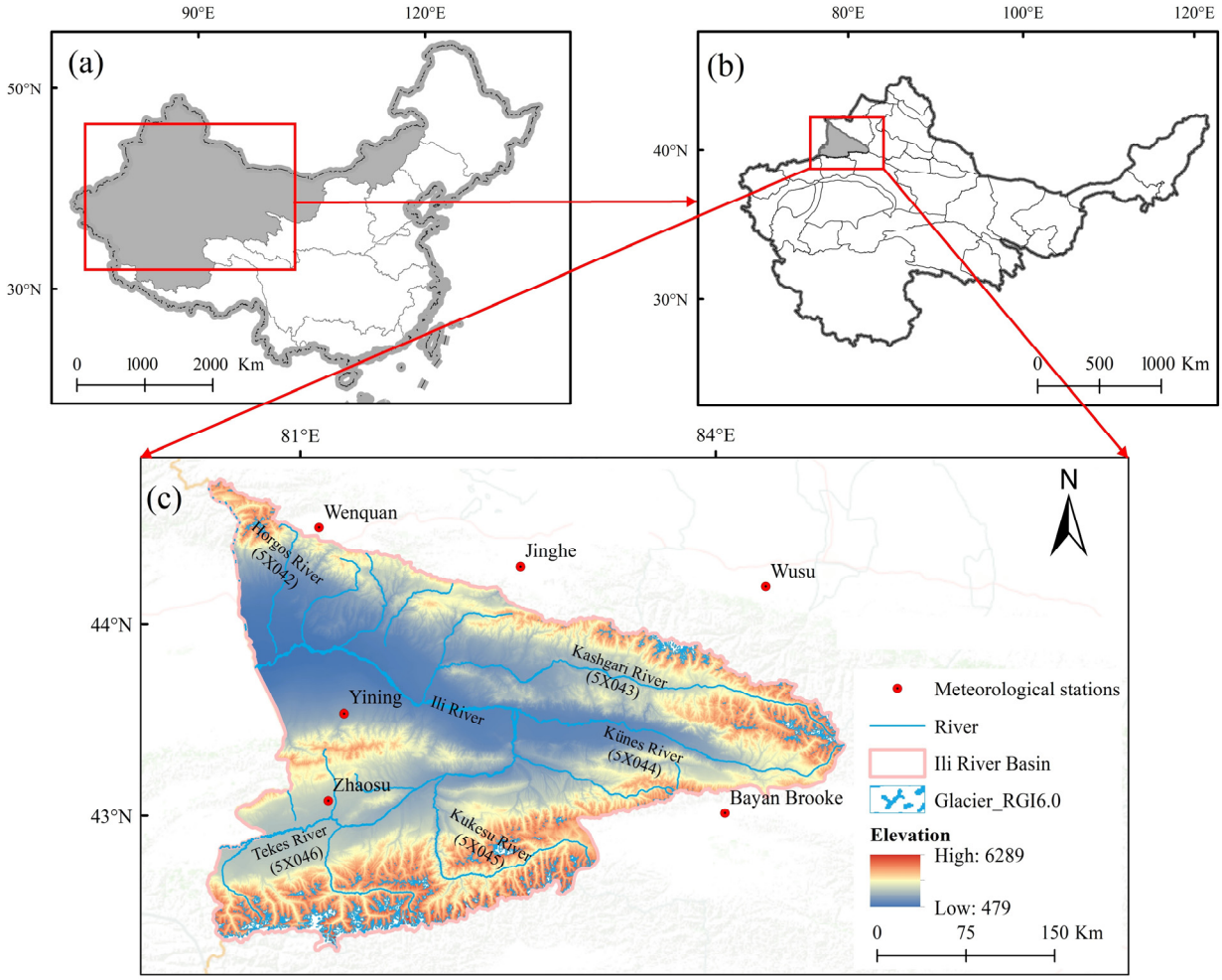


Figure 1. Study area. (**a**–**c**) denote the northwest arid region of China, the location of Ili River Basin, and the terrain and hydrological characteristics of the Ili River Basin.

2.2. Data Collection

2.2.1. Remote-Sensing Data

The primary data source for this research consisted of Landsat remote-sensing images with a spatial resolution of 30 m and a temporal resolution of 16 days. The global Landsat 5 data from 1992 to 2012 and Landsat 8 data from 2013 to 2020 were accessed through the GEE platform. The Landsat 5 and 8 datasets were preliminarily filtered for time, spatial extent, and cloud cover (less than 50%) using GEE filtering commands, and a pixel-based cloud-masking algorithm was employed to create cloud-free images. Images were chosen at five-year intervals (1992, 1995, 2000, 2005, 2010, 2015 and 2020), and data from the target year along with two neighboring years were combined for image synthesis. In addition, owing to the lack of images for 1995 and 2005, data from 1996 and 2006 were used as replacements. Finally, 239 scenes from Landsat 5 TM for the years 1992, 1996, 2006, and 2010, and 154 scenes from Landsat 8 OLI for the years 2015 and 2020, were chosen. The images of summer (July to September) were selected to reduce the impact of seasonal differences. Detailed information on the number of effective image scenes used for each target year is shown in Figure 2.

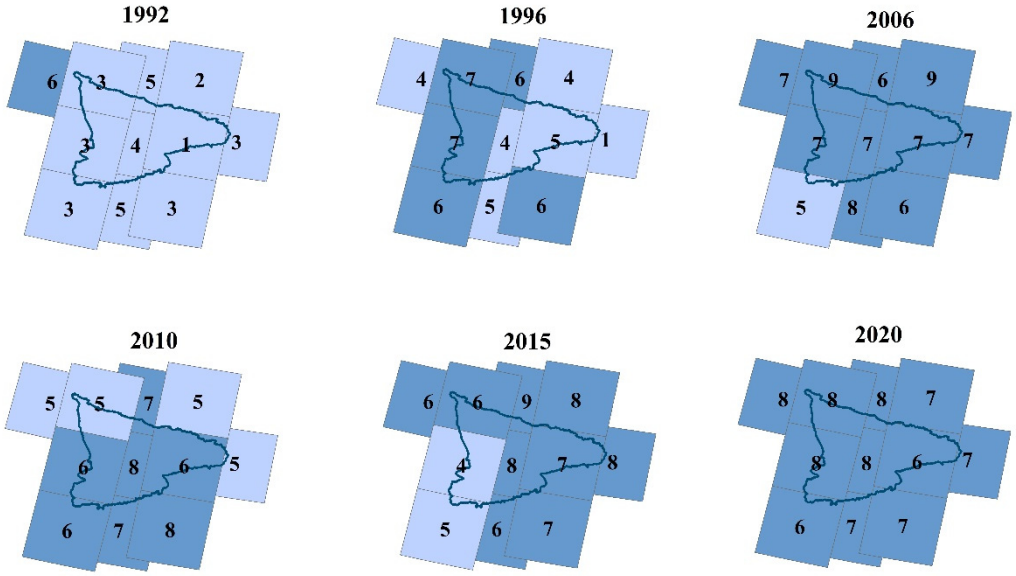


Figure 2. The number of valid Landsat images utilized for composite imagery synthesis for each target year. The blue lines outline the boundaries of the study area. The darker blue denotes that the number of available images is higher than five, while the lighter blue represents areas with fewer than five images.

2.2.2. Topographical, Land Cover and Meteorological Data

The present study used a Shuttle Radar Topography Mission (SRTM) digital elevation model (DEM) data to obtain topographical features, such as the slope, elevation, and aspect, to enhance classification precision. The Randolph Glacier Inventory (RGI, version 6.0) dataset was used as the boundary reference to evaluate changes in glacier area in the Ili River Basin. The boundary of the Ili River Basin, sourced from National Glacier Permafrost Desert Scientific Data Center (http://www.ncdc.ac.cn, accessed on 23 July 2022), included the boundaries, names, and coding of the basin divisions. The Chinese Yearly Land Cover Dataset (CLCD) [27] was selected for online assistance with sample data collection, as it covers the annual landcover information for China from 1985 to 2020, achieving an overall accuracy of 80%.

The meteorological data used in this study are sourced from the China Meteorological Data Network (http://data.cma.cn/, accessed on 28 July 2022), including annual and monthly datasets of ground climate data in China, used for analyzing information such as annual average temperature and annual precipitation. The meteorological data selected include six weather stations: Yining, Zhaosu, and the nearby Bayanbulak, Jinghe, Wenquan, and Wusu. The records from Yining, Zhaosu, Wenquan, and Wusu extend up to 2017, while those for Jinghe and Bayanbulak are traceable until 2020. The locations of these meteorological stations are illustrated in Figure 1.

2.3. Model Construction

2.3.1. Training Sample Selection

The quality of sample data is crucial in supervised classification, as it directly im-pacts the precision of the classification outcomes. In this study, we selected five land-cover types for model training: glacier, vegetation, water, built-up land, and barren land. To create a reliable sample library for training and validation, we combined land-use data from the CLCD with glacier data from RGI 6.0. For the glacier category, we specifically selected samples where the corresponding pixels were present in both the CLCD and RGI 6.0 datasets. However, for different years, some pixels were classified under different land-cover types. To ensure consistency, we removed these inconsistent pixels, resulting in a final sample set divided into 70% for training and 30% for validation. Ultimately, the total number of samples used was 4740, distributed as follows: 1413 for glacier, 1054 for

vegetation, 426 for water, 826 for built-up land, and 1021 for barren land. All spatial analyses and image processing were conducted using ArcMap (version 10.8.2, Esri, Redlands, CA, USA) and ERDAS IMAGINE (version 2022, Hexagon Geospatial, Madison, AL, USA).

2.3.2. Feature Construction

In the development of the classification feature set, we integrated spectral, index, textural, and topographic characteristics. The spectral features encompassed surface reflectance from Landsat 5 and Landsat 8, comprising seven bands: coastal, blue, green, red, near-infrared, and two shortwave infrared bands. The index features (Table 1) consisted of the normalized difference vegetation index (NDVI), NDSI, normalized difference snow and ice index (NDSII), normalized difference glacier index (NDGI), normalized difference water index (NDWI), normalized difference built-up index (NDBI), land surface water index (LSWI), and land surface temperature (LST). Texture, a key feature that depicts the spatial distribution of adjacent pixel brightness, was described using the gray-level cooccurrence matrix (GLCM) proposed by Haralick in 1973 [28]. For appropriate texture feature selection, we employed the Jeffries–Matusita (JM) distance feature optimization method [29], selecting 10 texture features that exceeded the mean: contrast (CON), variance (VAR), angular second moment (ASM), difference variance (DVAR), sum average (SAVG), sum variance (SVAR), shade (SHADE), prominence (PROM), inertia (INERTIA), and dissimilarity (DISS). The acquisition of terrain features relied on SRTM DEM data provided by the GEE cloud platform, which was used to extract the elevation, slope, aspect, and mountain shadows in the Ili River Basin. In conclusion, 29 features were chosen, comprising 7 spectral features, 8 index features, 10 texture features, and 4 terrain features, to characterize the variations in land-cover types within the Ili River Basin.

Table 1. Spectral index.

Name	Description	Formula
NDSI	Normalized difference snow index, used to distinguish between snow and ice-covered areas	$NDSI = \frac{\rho_{green} - \rho_{SWIR1}}{\rho_{green} + \rho_{SWIR1}}$
NDSII	Normalized difference snow and ice index, used in glacier range extraction and has good results	$NDSII = \frac{\rho_{red} - \rho_{SWIR1}}{\rho_{red} + \rho_{SWIR1}}$
NDGI	Normalized difference glacier index, used the green and red spectral bands to detect and monitor glaciers	$NDGI = \frac{\rho_{green} - \rho_{red}}{\rho_{green} + \rho_{red}}$
NDWI	Normalized difference water index, used to extract water bodies	$NDWI = \frac{\rho_{green} - \rho_{NIR}}{\rho_{green} + \rho_{NIR}}$
NDBI	Normalized difference building index, used to extract impervious surfaces	$NDBI = \frac{\rho_{SWIR1} - \rho_{NIR}}{\rho_{SWIR1} + \rho_{NIR}}$
NDVI	Normalized difference vegetation index, used to enhance the difference between vegetation and other feature types	$NDVI = \frac{\rho_{NIR} - \rho_{red}}{\rho_{NIR} + \rho_{red}}$
LSWI	Land surface water index, used to reflect the distribution and change in surface water	$LSWI = \frac{\rho_{NIR} - \rho_{SWIR1}}{\rho_{NIR} + \rho_{SWIR1}}$
LST	Land surface temperature	$LST = \frac{K_2}{\ln\left(\frac{K_1}{B(T_s)} + 1\right)}$

2.3.3. Jeffries–Matusita Distance

In this study, the JM distance was employed as the criterion for feature selection to build a classification feature set. The JM distance is a critical metric for assessing the separability between classes, and its primary purpose is to measure the distance between interclass samples to evaluate the separability between different categories, thus identifying which features are more discernible for training samples. It ranges from [0 to 2], with values closer to 2 indicating stronger separability between the categories [29]. When extracting GLCM texture features from Landsat images, the factors to consider include the choice of multiband combinations and various texture metrics, which were computed using Equations (1) and (2) as follows:

$$B = \frac{1}{8}(m_1 - m_2)^2 \frac{2}{\sigma_1^2 + \sigma_2^2} + \frac{1}{2}\ln\left[\frac{\sigma_1^2 + \sigma_2^2}{2\sigma_1\sigma_2}\right] \quad (1)$$

$$JM = 2\left(1 - e^{-B}\right) \quad (2)$$

where B represents the Bhattacharyya distance [30], and m_k and ${\sigma_k}^2$ represent the mean and variance of feature, where (k = 1, 2). The e in the formula usually represents the base of the natural logarithm (Euler's number), which is approximately equal to 2.71828.

In this study, the JM distance for individual features was firstly calculated, followed by the calculation of the average JM distance for same-class features and the removal of features below this average to optimize the same-class feature set. Ultimately, by combining features from different categories, the feature combination with the highest JM distance was chosen for classification. With the efficient computing capabilities of the GEE platform, this study aimed to explore the optimal feature combination method through JM distance calculations to enhance the classification accuracy and achieve superior classification outcomes.

2.3.4. Random Forest Algorithm

The RF algorithm, a typical machine learning approach, has demonstrated superior performance compared with other methods for glacier extraction [31]. In this study, we employed the RF algorithm from the GEE platform using the ArcGIS API for JavaScript (version 4.26, Esri, Redlands, CA, USA) to write a code that evaluates the impact of different number of decision trees on the classification accuracy of the RF model [32]. Taking 2020 as an example and using a step of 20, the parameters "number of Trees = 20, 40, 60, . . ., 300" were selected to determine the most beneficial number of decision trees. With the increase in the number of decision trees, the overall accuracy of the classification also increased [33]. When the number of trees reached 280, the values of OA (overall accuracy) and Kappa were the highest (Figure 3). Therefore, this study uses "number of Trees = 280" as the parameter for the random forest classification of 2020.

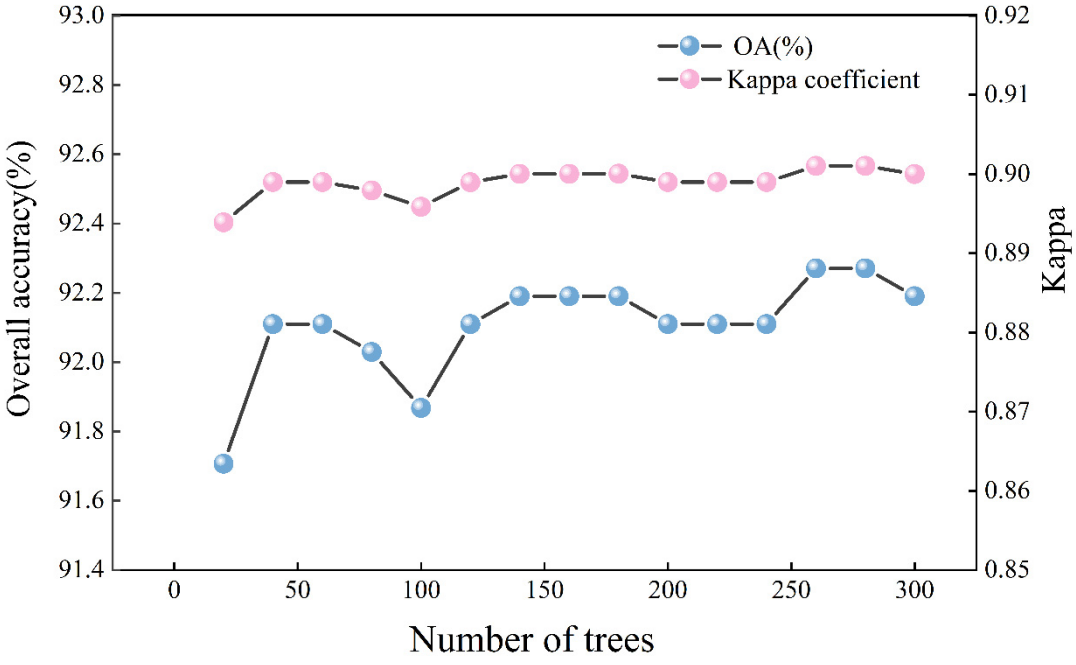


Figure 3. Variation in accuracy with number of trees (random forest).

3. Results

3.1. Feature Selection Optimization

Utilizing the GEE platform, we implemented a JM distance analysis with the average values of various category samples to assess the classification effectiveness of different features in extracting glacier information. Focusing on the separability between glaciers and other land-cover categories, we computed the JM distance between glaciers and other land-cover types as a measure of feature distinguishability. Features were progressively included from the highest to the lowest separability, and variations in glacier mapping

accuracy were monitored simultaneously (Figure 4). The analysis indicated that the mapping accuracy peaked when the number of features reached 23, with 10 texture features (PROM, SHADE, DVAR, CON, INERTIA, VAR, SVAR, DISS, SAVG, ASM, 2 terrain features (elevation, slope), 5 spectral features (B1–5), and 6 index features (NDSI, NDSII, LST, NDWI, NDVI, NDBI). The statistical analysis shown in Table 2 precisely delineates the JM distances of the 23 features and reveals their varying roles in distinguishing glaciers from other land features. Among these features, the texture features exhibiting the greatest separability, followed by spectral, index, and terrain features. Among the texture features, the contrast attribute of NDSI (NDSI_Prom) exhibited the best performance, and its correlation feature (NDSI_Corr) was relatively weaker. Regarding the spectral features, the degree of separation of band1 was the highest, whereas that of band 7 was relatively lower. Among index features, the NDSI excelled, whereas the NDGI was less impressive. Although the separability of terrain features lagged behind that of the other features, they still played a crucial role in glacial information extraction. Generally, the distinct color and texture characteristics of glacier surfaces offer clear indicators for effectively distinguishing them from other land categories.

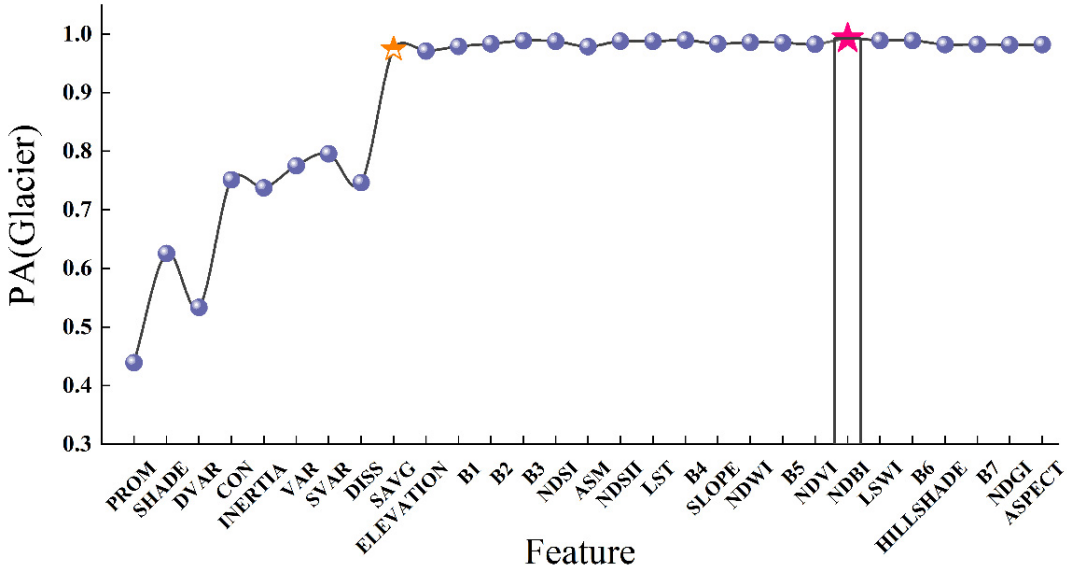


Figure 4. Variation in glacier producer accuracy (PA) with different features. The vertical columns indicate the specific features where significant changes in PA are observed. The yellow star denotes the feature where PA reaches near-perfect accuracy, indicating its highest contribution to the model's performance. The red star represents the point beyond which adding more features does not significantly improve PA, suggesting an optimal feature set for the model.

Table 2. Jeffries–Matusita distance between different types of features.

Feature	Highest Separability	Lowest Separability	Mean Jeffries–Matusita Distance
Texture features	PROM	ASM	1.841
Spectral features	B1	B7	1.162
Index features	NDSI	NDGI	1.058
Terrain features	Elevation	Aspect	0.884

3.1.1. Postprocessing after Classification

The post-image classification analysis identified fragmented patterns and 'misclassification noise'. To mitigate these issues and boost classification precision, we employed the majority filter tool for spatial smoothing using an 8-neighbor majority filtering. Subsequently, a boundary cleaning tool was utilized to merge the scattered patches and smooth their edges. A minimum size threshold of 0.01 km^2 (equivalent to about 11 pixels in Landsat

imagery) was set to exclude overly small, isolated patches. Finally, the Nibble tool was employed to substitute the values of the raster pixels within the mask area with those of the nearest points, thereby further refining the classification result. After these processing steps, optimized classification maps of the Ili River Basin for six periods (1992, 1996, 2006, 2010, 2015, and 2020) were acquired, as shown in Figure 5, with 2020 as the case.

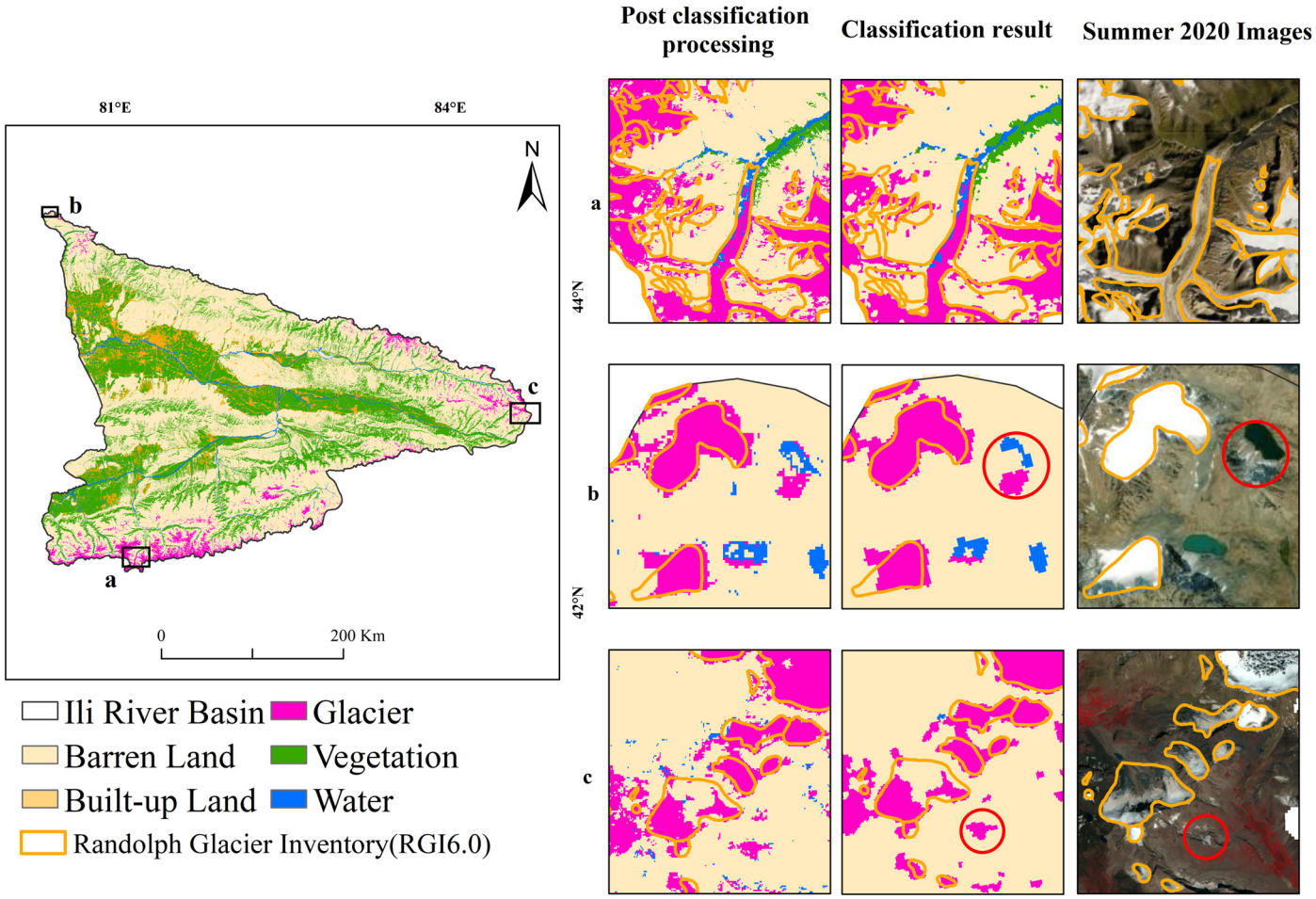


Figure 5. Three subsets of remote-sensing image (**a**–**c**) and their classification results for 2020. The orange lines represent the boundaries of glaciers as defined by the Randolph Glacier Inventory (RGI 6.0). The red circles highlight areas of discrepancies between the classification results and the RGI, indicating regions where manual inspection or further refinement may be necessary.

3.1.2. Accuracy Evaluation

The glacier classification results for the Ili River Basin for 1992, 1996, 2006, 2010, 2015, and 2020 derived from the RF algorithm and post-classification processing are demonstrated in Figure 6. Glaciers are primarily scattered along the northern slopes of the Harktu Mountains to the south of the study area. Confusion matrices for the six target years derived from the GEE platform revealed that the OA, UA, producer accuracy (PA), and kappa coefficient (Figure 7) were commendable. Moreover, the kappa coefficients for each target year exceeded 85%, clearly demonstrating the robustness of RF algorithm. Regarding glacier classification, the high UA and PA, both exceeding 90%, highlight the effectiveness of the method in discriminating between glacier and nonglacial categories.

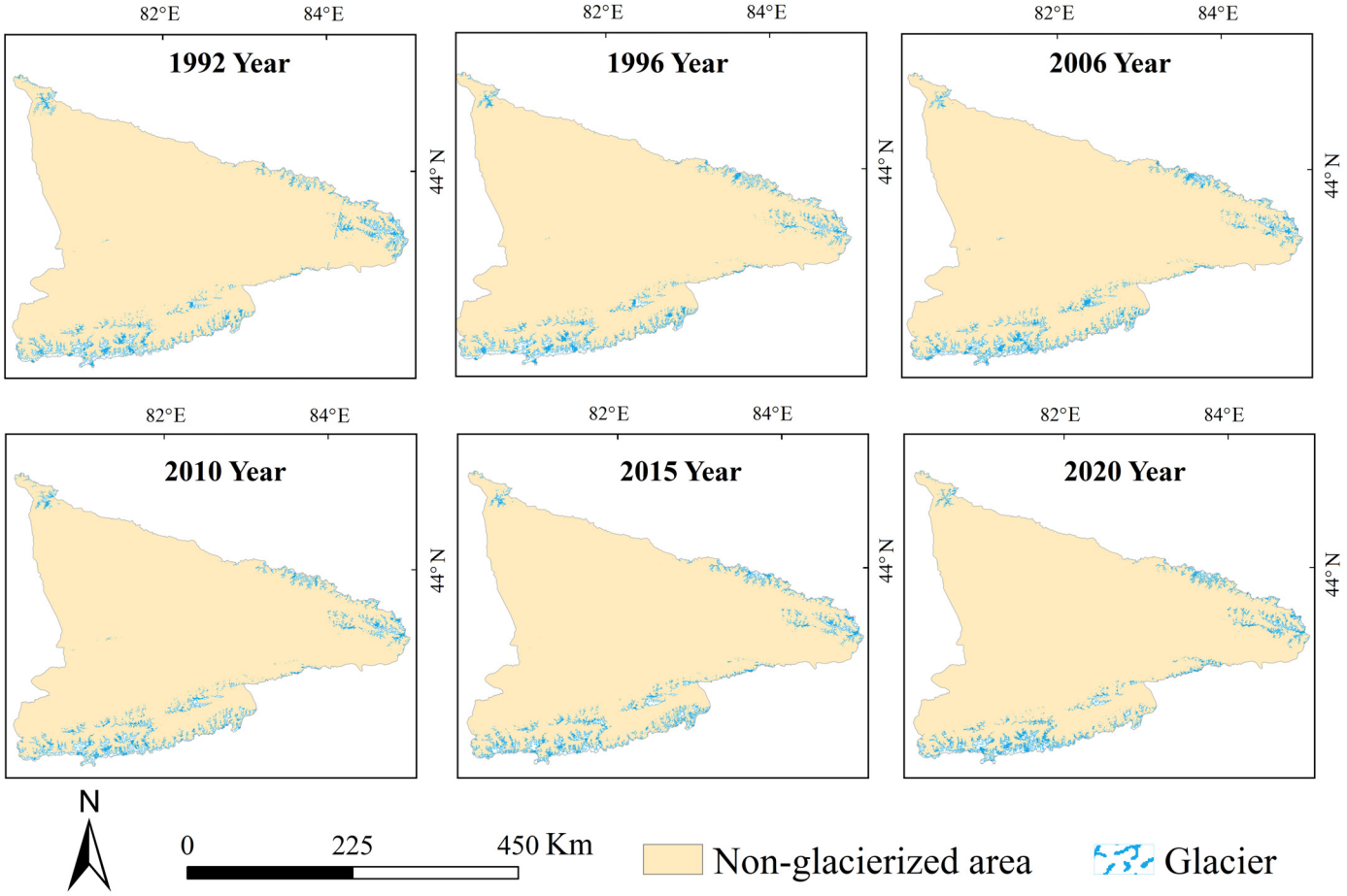
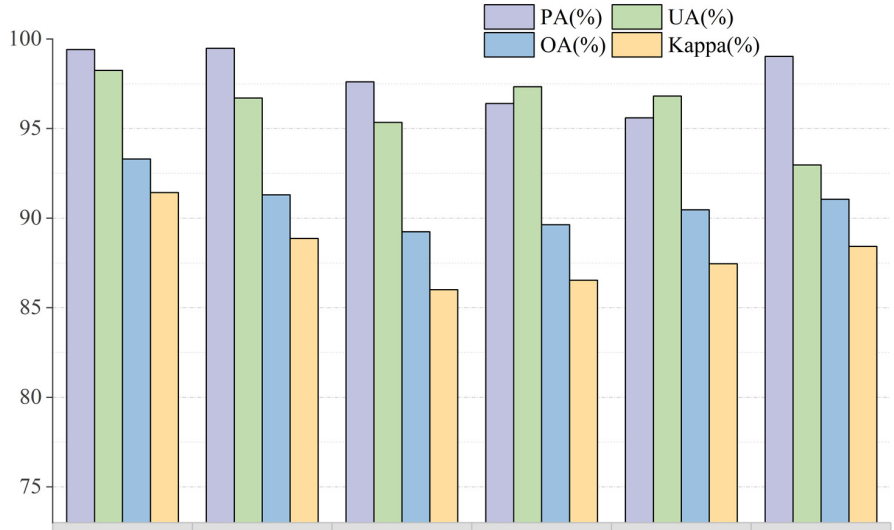


Figure 6. Distribution of glacier area in the Ili River Basin during 1992–2020.



Year	2020	2015	2010	2006	1996	1992
Kappa(%)	91.43	88.87	86.01	86.53	87.45	88.42
OA(%)	93.3	91.3	89.24	89.63	90.47	91.05
UA(%)	98.25	96.71	95.34	97.34	96.82	92.97
PA(%)	99.41	99.48	97.61	96.4	95.6	99.03

Figure 7. The classification accuracy of glacier data in the Ili River Basin during 1992–2020 using the Google Earth Engine (GEE) platform. OA, overall accuracy; UA, user accuracy; PA, producer accuracy.

3.2. Glacier Distribution and Changes in the Ili River Basin

During the study period, glaciers in the Ili River Basin have exhibited an overall decreasing trend (Table 3), with a total retreat of 184.76 km^2, constituting 8.60% of the total glacier area in 1992. An additional analysis showed that the glacier retreat rates varied during different time periods. The period from 2006 to 2010 had the highest glacier retreat rate, whereas after 2010, the retreat rates were relatively lower. Specifically, during 1992–2020, the retreat rates for the periods 1992–1996, 1996–2006, 2006–2010, 2010–2015, and 2015–2020 were 0.17%/a, 0.34%/a, 0.74%/a, 0.10%/a, and 0.35%/a, respectively, suggesting that the glaciers in the Ili River Basin exhibited varying retreat rates at different stages.

Table 3. Distribution area and variation characteristics of glaciers in the Ili River Basin during 1992–2020.

Year	Area (km^2)	Area Change (km^2)	Rate of Change (km^2/a)	Rate of Area Change (%)	APAC (%/a)
1992	2148.65				
1996	2134.36	−14.29	−3.57	−0.66	−0.17
2006	2069.42	−64.95	−6.46	−3.04	−0.34
2010	2008.48	−60.94	−15.23	−2.94	−0.74
2015	1998.38	−10.10	−2.02	−0.50	−0.10
2020	1963.89	−34.49	−6.90	−1.73	−0.35

Using spatial analysis tools, we conducted a statistical analysis of the distribution of and variation in glaciers across various elevation bands and slopes in the Ili River Basin over the last three decades. The elevation range was segmented into 16 intervals, with the glacier areas within each elevation segment tabulated for six distinct time periods. The advancing or retreating trends in the glaciers at these elevations were analyzed (Figure 8). We discovered noticeable differences in the glaciers of the Ili River Basin at different elevations, which were generally consistent with the trends in elevation, demonstrating a distinct regularity. The specific pattern observed was as follows: with increasing elevation, the area occupied by glaciers expanded, but started to decrease after reaching a certain elevation. For each period, the largest glacier distribution area was consistently within the same elevation range (3800–3900 m). Glaciers at elevations below 4400 m predominantly exhibited a considerable retreating trend, with the largest shrinkage occurring between 3500 and 4400 m, representing approximately 98.26% of the total retraction in glacier area.

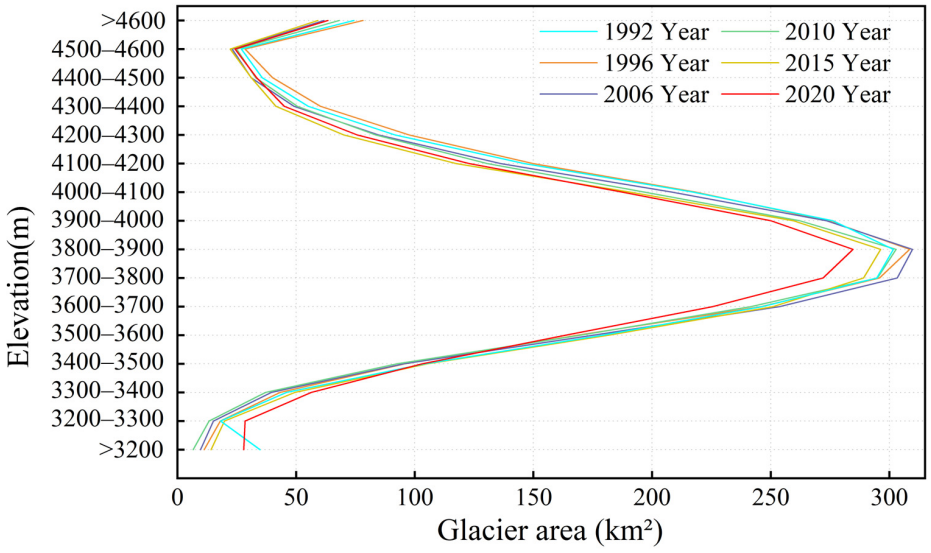


Figure 8. Variations in the areas of glaciers at different elevations in the Ili River Basin during 1992–2020.

During the study period, glaciers in various areas of the Ili River Basin have exhibited an intermittent retreating trend. Because of factors such as mountainous terrain, glacier areas vary among different slopes, with approximately 60% of the glaciers located on the north, southwest, west, and northwest aspects (Figure 9). For instance, in 1992, the glacier areas on the north, southwest, west, and northwest slopes were 524.24 km^2, 205.08 km^2, 297.35 km^2, and 557.07 km^2, respectively, representing 24.40%, 13.84%, 25.93%, and 14.33% of the total glacier area in that year's study area, respectively. The northwest slope had the largest glacier area among all aspects, whereas the east and southeast slopes had comparatively smaller glacier areas. Glaciers on the north, west, and northwest slopes had larger retreat rates, shrinking by 174.30 km^2 from 1992 to 2020, with a notable decline after 2006. In contrast, glacier areas on the east, northeast, and south slopes demonstrated a consistent declining trend before 2010, followed by an expanding trend between 2010 and 2020.

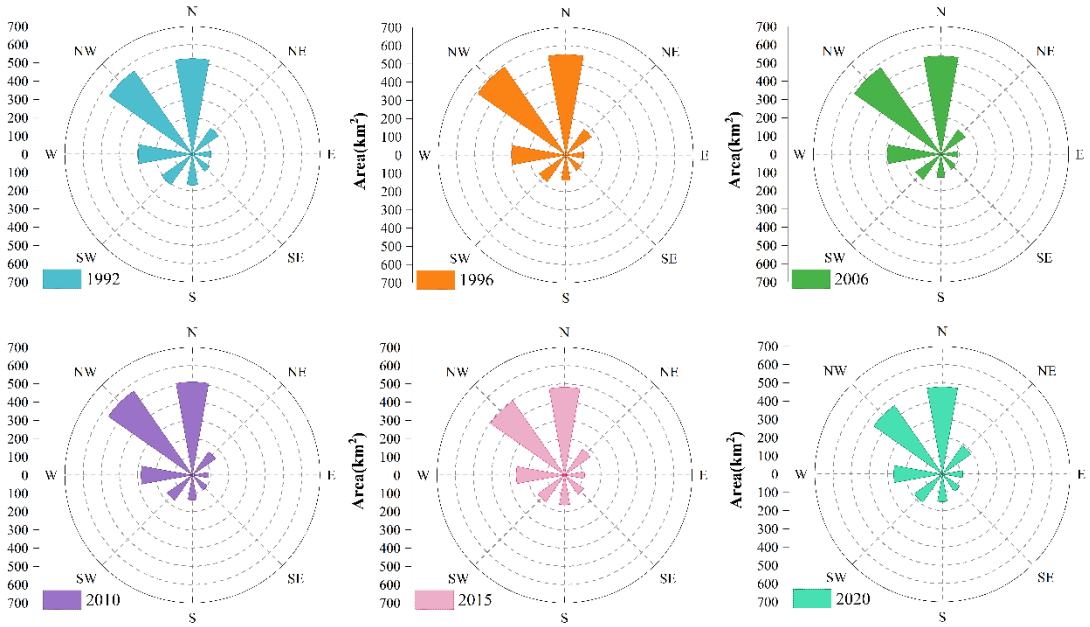


Figure 9. Directional variation in glaciers in the Ili River Basin during 1992–2020.

4. Discussion

4.1. Glacier Retreat Area

As remote-sensing technology advances, glacier monitoring research has gained renewed vigor. Especially in Western China, a multitude of studies have deeply analyzed the regional glacier retreat conditions. It was reported that over the past twenty years, glaciers in Western China have experienced an annual retreat rate of up to 1.46% [34]. This finding highlights that the glaciers in regions such as the Qilian Mountains, Altai Mountains, and Tianshan Mountains are all in a state of accelerated retreat. Owing to their distinctive geographical and climatic conditions, the Tianshan Mountains exhibit notable differences in glacier retreat rates. Numerous studies have shown that, over recent decades, glaciers in different subsections of the range have experienced average retreat rates oscillating between 0.27%/a and 0.92%/a, clearly emphasizing the substantial role of geographical factors in glacier retreat [35,36]. In particular, the eastern glaciers of the Tianshan Mountains are retreating most quickly, the north follows, and the west is comparatively slow, correlating not only with regional variations in precipitation and temperature but also mirroring differences in glacier attributes and climate interplay.

Regarding the Ili River Basin glaciers, previous studies observed that the glacier area in the Ili River Basin decreased by approximately 0.2% each year [34], while Xu et al. [25] reported a faster retreat rate of approximately 0.6%/a [37]. The results of our study are more closely aligned to those of the former study, showing an average annual decrease

of approximately 0.29% in the glacier area of the Ili River Basin. The presence of these differences can be attributed to the use of various glacier datasets and the choice of different study periods. To thoroughly investigate the dynamics of glacier changes in the Ili River Basin, our research has undertaken a comparative analysis with the glacier change trends from other areas of the Tianshan (Table 4). The corresponding results reveal that the rate of glacier retreat in the Ili River Basin was relatively lower compare with other regions of the Tianshan Mountains. The differences in glacier retreat rates across the Tianshan Mountains and other regions of Western China (as seen in Table 4) reflect the complex interactions between regional climate patterns and local glacier dynamics. The slower retreat in the Ili River Basin compared to other parts of the Tianshan could be due to differences in topography, local climatic conditions, and glacier characteristics, such as size and altitude. Globally, similar patterns of varying retreat rates are observed, where regional differences in climate change impacts, such as temperature increases and precipitation patterns, lead to differing glacier responses [38].

Table 4. Comparison of glacier changes in typical areas of western China.

Period	Specific Region	Average Area Changes Rate (%/a)	References
2000–2020	Western China	1.46	[39]
1987–2018	Western China	0.99	[40]
1989–2016	Sugan Lake Basin	0.5	[41]
1960–2009	Western China	0.75	[42]
1990–2021		0.55	
1989–2011	Western China	−0.64	[43]
1990–2000	Western China	−0.8	[44,45]
2001–2021		−1.56	
1990–2018	Western China	−0.44	[44]
2000–2010		−0.22	
2000–2007	Pskem region	−0.71	[43]
1986–2000	Kaidu Kongque River Basin	−0.35	[46]
2000–2020		−0.26	
1975–2016	Aksu River Basin	−0.63	[45,47]
2001–2011		−0.66	
2011–2021		−0.88	
1956–2008	Upper Ili glacier system in China	−0.73	[48]
1992–2010	Ili River Basin	−0.36	This study
2010–2020		−0.22	

4.2. Uncertainties

In this study, the spatio-temporal variations of glaciers in the Ili River Basin were investigated using the GEE platform and the RF algorithm. As a robust public database, the GEE platform offers extensively used remote-sensing image data and facilitates the efficient processing of large-scale, multisource data. Given its advantages over traditional image processing tools in terms of processing speed and data volume, this platform represents an important opportunity and introduces new challenges to glacier remote-sensing [49]. The RF algorithm is regarded as one of the most efficient algorithms for land-cover classification using remote-sensing data in regions with complex topography [50]. Unlike other widely used classifiers, it is typically less affected by data noise and overfitting, showing greater classification accuracy in a variety of application contexts [51]. However, while the OA indicates the ratio of correctly classified image elements to the total number of image elements, a high OA might conceal the low accuracy in specific categories caused by sample imbalance during classification. Therefore, the kappa coefficient is an essential supplementary measure. It is a consistency test coefficient, based on the confusion matrix [52], that offers a more comprehensive reflection of the consistency between the sampled areas and the actual sampled areas in glacier information extraction, enabling a more accurate

evaluation of the precision of the method. In our research, the use of both OA and the kappa coefficient revealed higher confidence intervals, demonstrating that the extracted glacier information aligned well with the reference data.

Moreover, we found that the distribution of the glaciers we assessed in this study was affected by various factors such as the quality of the image input data, the representativeness of the sample data, and the suitability of the land-cover classification scheme. This emphasizes the importance of employing advanced tools and algorithms for glacier monitoring and highlights the need for meticulous data and method selection in similar studies. To enhance the quality of the classification maps, we employed an OA band to eliminate most of the invalid pixels from the composite images. Although this approach effectively eliminates a considerable number of invalid pixels, band limitations prevent the complete removal of all invalid pixels [53,54], potentially resulting in lower-quality composite images and increased uncertainty in classification. Various landcover classification systems can yield diverse results. This study primarily focused on the changes in glacier area and not on detailed surface-cover classification. Consequently, we simplified the classification results into two broad categories: glacier and nonglacial. Although this classification method simplified the analysis, it adequately met the study's focus and analytical requirements for glacier area changes.

4.3. Response of Glacier Variations to Climate Change

During the past few decades, there has been a marked global retreat of glaciers, with the area shrinkage rate in 16 major glacier zones reaching 11.3% [55]. In particular, research on the Tibetan Plateau and adjacent regions indicates that glaciers in several areas such as the Himalayas, Qilian Mountains, and Western Tianshan are extremely sensitive to changes in temperature [39]. Similarly, Xinjiang has experienced a notable rise in temperature and precipitation over the last half-century [56]. Glaciers are exceedingly sensitive to a variety of climate changes, particularly the key climatic factors of precipitation and temperature, which directly influence glacier formation and evolution [57]. Increases in temperature can result in the melting of glaciers, whereas augmented precipitation may aid in glacier accumulation [58]. In terms of spatial distribution, glacier changes show clear regional disparities that are largely affected by the topography, terrain, and size of the glaciers [59]. Temporally, the influence of climatic factors on glacier changes cannot be overlooked. Generally, glaciers exhibit lagged responses to climate change, with different glacier types exhibiting diverse lag times in responding to these changes [60]. The Ili River Basin mainly consists of smaller glaciers with areas mostly less than 1 km^2, making them more responsive to climate variations. Moreover, the exact lag time could not be determined due to the absence of field observation data. Hence, in this study, we temporarily disregarded the lag effect of climate change on glaciers.

Given that the Ili River Basin only has two meteorological observation stations, Yining and Zhaosu, we opted to include four nearby stations, Bayanbulak, Jinghe, Wenquan, and Wusu, and integrated data from these stations to represent the climate changes more comprehensively in the study area. Analyzing the changes in temperature and precipitation (Figure 10) revealed that, during 1992–2020, there was a slight increase in both the annual average temperature and annual precipitation, exhibiting complex variability from 1992 to 2020. In detail, the annual average temperature rose by 0.26 °C, with a warming rate of 0.1 °C/10 a ($p < 0.05$), whereas the trend in annual precipitation during the same timeframe was less pronounced. Between 1992 and 1996, there was a gradual decline ($p < 0.05$) in the annual average temperature, reaching a low of 4 °C. During this period, the annual precipitation exhibited a fluctuating increase, reaching a peak in 1993. Between 1996 and 2010, the annual average temperature displayed a fluctuating rise ($p < 0.05$), achieving a relatively high level of 6.14 °C in 2007 and then slightly declining. Meanwhile, there was a general downward trend in annual precipitation, with the lowest in 2008, followed by an annual increase, peaking in 2010. Between 2010 and 2015, the average annual temperature exhibited a fluctuating decrease ($p < 0.05$). In 2015, the annual average temperature reached

a high point (6.16 °C). In this phase, despite fluctuations, the annual precipitation exhibited an overall increasing trend. Between 2015 and 2020, the average annual temperature fluctuated, rising slightly ($p < 0.05$). Conversely, the annual precipitation in 2016 reached its highest level in nearly 30 years (393.15 mm).

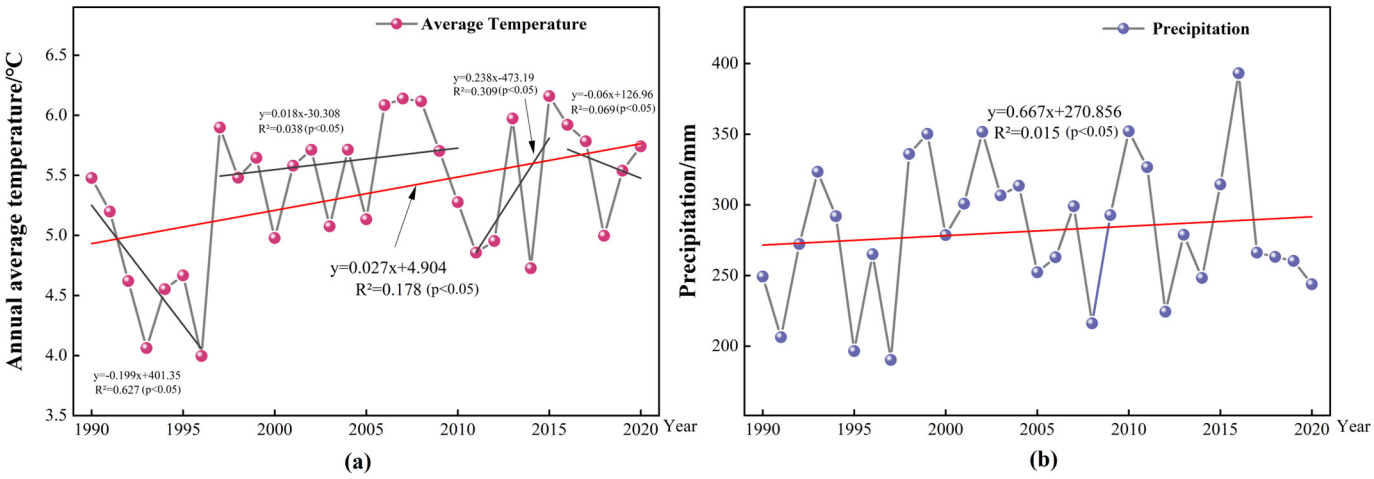


Figure 10. Annual air temperature and (**a**) and annual precipitation (**b**) in the Ili River Basin from 1992 to 2020. The red lines denote long term trend.

Between 1992 and 2020, the glaciers in the Ili River Basin consistently shrank (Table 3), and there was a noticeable increase in the annual average temperature during the same period (Figure 10). The glacier retreat rate closely corresponded to the trends in temperature and precipitation. Between 1996 and 2010, there was a notable correlation between the swift retreat of glaciers and the rapid rise in the annual average temperature. After 2015, the trend in increasing temperatures leveled off, and the rate of glacier retreat stabilized. Specifically, from 2006 to 2010, the heightened rate of glacier retreat could be linked to the unusually high temperatures in those years, which occasionally surpassed 6 °C. Notably, between 2010 and 2015, although there was a clear increase in temperature and a marked decrease in annual precipitation, the change in glacier area was not substantial. This indicates that there may be a delay in the response of glaciers to rising temperatures. Therefore, there was no noticeable change in glacier area during this period. The likely reason for this is a time delay in the glacier response, leading to no apparent changes in the glacier area in the short term.

Globally, glaciers are retreating at an accelerated rate due to rising temperatures driven by anthropogenic climate change. This trend has been observed in mountain ranges across the world, including the Andes [38], the Alps [61], and the Himalayas [62]. The accelerated melting of glaciers contributes significantly to global sea-level rise and poses a risk to freshwater resources in regions that rely on glacial meltwater for irrigation, drinking water, and hydropower. The glacier retreat in the Ili River Basin, while slower compared to other regions of the Tianshan, still contributes to the overall global trend in glacier mass loss. The consistent reduction in glacier area over the past decades highlights the sensitivity of glaciers to temperature increases. The relatively lower retreat rate in the Ili River Basin suggests that, while this region might experience less immediate impact, it is still part of the broader global phenomenon of glacial decline [47]. This finding underscores the importance of continued monitoring and research to understand the long-term impacts of climate change on glacier dynamics and water resources in both regional and global contexts.

5. Conclusions

Utilizing the robust computational power of the GEE cloud platform, this study employed online programming to access Landsat 5, Landsat 8, and topographical data to

extract spectral, textural, and topographic features. The JM distance algorithm was used for feature optimization, combined with the RF classification method, to extract changes in glaciers in the Ili River Basin during 1992–2020, resulting in detailed classification maps. Our main findings were as follows:

(1) The JM distance analysis conducted on the GEE platform revealed that optimal mapping accuracy was achieved when 23 features were used.
(2) The overall classification accuracies for the period 1992–2020 all exceeded 89%, and the Kappa coefficients all exceeded 85%, especially for the glacier category, where both the user and producer accuracies exceeded 90%. This verifies the high reliability of the RF algorithm in terms of spatial continuity and boundary clarity.
(3) During 1992–2020, the glaciers in the Ili River Basin showed a decreasing trend, with a total reduction of 184.76 km^2 in area and an average annual retreat rate of 6.84 km^2/a. The retreat rate was most significant from 2006 to 2010, and was more pronounced at lower elevations and on the northern slopes. The impact of climate change on small glaciers is more significant.
(4) From 1992 to 2020, the climate change in the study area shows complex fluctuations; the mean annual temperature increased by 0.26 °C, while the trend in annual precipitation was not obvious during the same period. The rate of glacier retreat is closely related to the rapid increase in temperature. Despite the continued increase in temperature from 2010 to 2015, the change in glacier area was not significant, indicating a certain lag in the response of glaciers to climate change.

Author Contributions: Conceptualization, Z.X. and Y.W.; methodology, Q.Z., Z.Z. and X.W.; software, Q.Z., Z.Z. and X.W.; validation, Q.Z., Z.Z. and X.W.; formal analysis, Z.Z.; investigation, Q.Z. and Z.Z.; resources, Y.W.; writing—original draft preparation, Q.Z., Z.Z., X.W. and Z.X.; writing—review and editing, Q.Z., Z.Z., X.W. and Z.X.; visualization, Z.Z.; supervision, Z.X. and Y.W.; project administration, Z.X. and Y.W.; funding acquisition, Z.X. and Y.W. All authors have read and agreed to the published version of the manuscript.

Funding: This research was funded by Natural Science Foundation of Xinjiang Uygur Autonomous Region (No. 2022E01052, No.2022D01B234 and No. 2023E01006).

Data Availability Statement: The original contributions presented in this study are included in the article. Further inquiries can be directed to the corresponding author.

Conflicts of Interest: The authors declare no conflicts of interest.

References

1. Karthe, D.; Chalov, S.; Borchardt, D. Water resources and their management in central asia in the early twenty first century: Status, challenges and future prospects. *Environ. Earth Sci.* **2015**, *73*, 487–499. [CrossRef]
2. Ding, Y.; Liu, S.; Li, J.; Shangguan, D. The retreat of glaciers in response to recent climate warming in western china. *Ann. Glaciol.* **2006**, *43*, 97–105. [CrossRef]
3. Zhengyong, Z.; Lin, L.; Xinlin, H.E.; Zhongqin, L.I.; Puyu, W. Evaluation on glaciers ecological services value in the tianshan mountains, northwest China. *J. Geogr. Sci.* **2019**, *029*, 101–114.
4. Oerlemans, J. Extracting a climate signal from 169 glacier records. *Science* **2005**, *308*, 675–677. [CrossRef]
5. Vuille, M.; Francou, B.; Wagnon, P.; Juen, I.; Kaser, G.; Mark, B.G.; Bradley, R.S. Climate change and tropical andean glaciers: Past, present and future. *Earth Sci. Rev.* **2008**, *89*, 79–96. [CrossRef]
6. Shiyin, L.; Wenxin, S.; Yongping, S.; Gang, L. Glacier changes since the little ice age maximum in the western qilian shan, northwest china, and consequences of glacier runoff for water supply. *J. Glaciol.* **2003**, *49*, 117–124. [CrossRef]
7. Yao, T.; Thompson, L.; Yang, W. Different glacier status with atmospheric circulations in tibetan plateau and surroundings. *Nat. Clim. Change* **2012**, *2*, 663–667. [CrossRef]
8. Jianping, D.; Lily, W.; Jiawen, R.; Lun, L.I. Seasonal variations in heavy metals concentrations in mt. Qomolangma region snow. *J. Geogr. Sci.* **2009**, *19*, 249–256.
9. Racoviteanu, A.E.; Williams, M.W.; Barry, R.G. Optical remote sensing of glacier characteristics: A review with focus on the himalaya. *Sensors* **2008**, *8*, 3355–3383. [CrossRef]
10. Paul, F.; Barrand, N.E.; Baumann, S.; Berthier, E.; Bolch, T.; Casey, K.; Frey, H.; Joshi, S.; Konovalov, V.; Le Bris, R. On the accuracy of glacier outlines derived from remote-sensing data. *Ann. Glaciol.* **2013**, *54*, 171–182. [CrossRef]

11. Bamber, J.L.; Rivera, A. A review of remote sensing methods for glacier mass balance determination. *Glob. Planet. Change* **2007**, *59*, 138–148. [CrossRef]
12. Cox, L.H.; March, R.S. Comparison of geodetic and glaciological mass-balance techniques, gulkana glacier, alaska, USA. *J. Glaciol.* **2004**, *50*, 363–370. [CrossRef]
13. Huss, M. Density assumptions for converting geodetic glacier volume change to mass change. *Cryosphere* **2013**, *7*, 877–887. [CrossRef]
14. Chen, F.; Zhang, M.; Tian, B.; Li, Z. Extraction of glacial lake outlines in tibet plateau using landsat 8 imagery and google earth engine. *IEEE J. Sel. Top. Appl. Earth Obs. Remote Sens.* **2017**, *10*, 4002–4009. [CrossRef]
15. Johnson, B.A.; Iizuka, K. Integrating openstreetmap crowdsourced data and landsat time-series imagery for rapid land use/land cover (lulc) mapping: Case study of the laguna de bay area of the philippines. *Appl. Geogr.* **2016**, *67*, 140–149. [CrossRef]
16. Hu, Y.; Hu, Y. Land cover changes and their driving mechanisms in central asia from 2001 to 2017 supported by google earth engine. *Remote Sens.* **2019**, *11*, 554. [CrossRef]
17. Huang, H.; Chen, Y.; Clinton, N.; Wang, J.; Wang, X.; Liu, C.; Gong, P.; Yang, J.; Bai, Y.; Zheng, Y. Mapping major land cover dynamics in beijing using all landsat images in google earth engine. *Remote Sens. Environ.* **2017**, *202*, 166–176. [CrossRef]
18. Wang, Y.D.; Li, Z.W.; Zeng, C.; Xia, G.S.; Shen, H.F. An urban water extraction method combining deep learning and google earth engine. *IEEE J. Sel. Top. Appl. Earth Obs. Remote Sens.* **2020**, *13*, 768–781. [CrossRef]
19. Liao, W.; Jiang, W. Evaluation of the spatiotemporal variations in the eco-environmental quality in china based on the remote sensing ecological index. *Remote Sens.* **2020**, *12*, 2462. [CrossRef]
20. Ermida, S.L.; Mantas, V.; Trigo, I.F. Google earth engine open-source code for land surface temperature estimation from the landsat series. *Remote Sens.* **2020**, *12*, 1471. [CrossRef]
21. Dong, J.; Xiao, X.; Menarguez, M.A.; Zhang, G.; Qin, Y.; Thau, D.; Biradar, C.; Moore, B. Mapping paddy rice planting area in northeastern asia with landsat 8 images, phenology-based algorithm and google earth engine. *Remote Sens. Environ.* **2016**, *185*, 142–154. [CrossRef]
22. Xiong, J.; Thenkabail, P.S.; Gumma, M.K.; Teluguntla, P.; Poehnelt, J.; Congalton, R.G.; Yadav, K.; Thau, D. Automated cropland mapping of continental africa using google earth engine cloud computing. *ISPRS J. Photogramm. Remote Sens.* **2017**, *126*, 225–244. [CrossRef]
23. Li, Z.; Abulikemu, A.; Zhu, K.; Mamtimin, A.; Zeng, Y.; Li, J.; Abulimiti, A.; Kadier, Z.; Abuduaini, A.; Li, C.; et al. Diurnal variation characteristics of summer precipitation and related statistical analysis in the ili region, xinjiang, northwest china. *Remote Sens.* **2023**, *15*, 3954. [CrossRef]
24. Guo, L.; Xia, Z. Temperature and precipitation long-term trends and variations in the ili-balkhash basin. *Theor. Appl. Climatol.* **2014**, *115*, 219–229. [CrossRef]
25. Xu, B.; Lu, Z.; Liu, S.; Li, J.; Xie, J.; Long, A.; Yin, Z.; Zou, S. Glacier changes and their impacts on the discharge in the past half-century in tekes watershed, central asia. *Phys. Chem. Earth Parts A/B/C* **2015**, *89–90*, 96–103. [CrossRef]
26. Sorg, A.; Bolch, T.; Stoffel, M.; Solomina, O.; Beniston, M. Climate change impacts on glaciers and runoff in tien shan (central asia). *Nat. Clim. Change* **2012**, *2*, 725–731. [CrossRef]
27. Yang, J.; Huang, X. The 30 m annual land cover dataset and its dynamics in china from 1990 to 2019. *Earth Syst. Sci. Data* **2021**, *13*, 3907–3925. [CrossRef]
28. Haralick, R.M.; Shanmugam, K.; Dinstein, I. Textural features for image classification. *Stud. Media Commun.* **1973**, *SMC-3*, 610–621.
29. Pengyu, H.; Li, W.; Yulin, Z.; Zheng, N. Using moderate-resolution temporal ndvi profiles for high-resolution crop mapping in years of absent ground reference data: A case study of bole and manas counties in xinjiang, china. *ISPRS Int. J. Geo-Inf.* **2016**, *5*, 67. [CrossRef]
30. Sifeng, B.; Matteo, B.; Michael, B. The role of the bhattacharyya distance in stochastic model updating. *Mech. Syst. Signal Process.* **2019**, *117*, 437–452.
31. Lu, Y.; Zhang, Z.; Kong, Y.; Hu, K. Integration of optical, sar and dem data for automated detection of debris-covered glaciers over the western nyainqentanglha using a random forest classifier. *Cold Reg. Sci. Technol.* **2022**, *193*, 103421. [CrossRef]
32. Xie, F.; Liu, S.; Gao, Y.; Zhu, Y.; Wu, K.; Qi, M.; Duan, S.; Tahir, A. Derivation of supraglacial debris cover by machine learning algorithms on the gee platform: A case study of glaciers in the hunza valley. *ISPRS Ann. Photogramm. Remote Sens. Spat. Inf. Sci.* **2020**, *3*, 417–424. [CrossRef]
33. Racoviteanu, A.; Williams, M.W. Decision tree and texture analysis for mapping debris-covered glaciers in the kangchenjunga area, eastern himalaya. *Remote Sens.* **2012**, *4*, 3078–3109. [CrossRef]
34. Wang, S.; Zhang, M.; Li, Z.; Wang, F.; Li, H.; Li, Y.; Huang, X. Glacier area variation and climate change in the chinese tianshan mountains since 1960. *J. Geogr. Ences* **2011**, *21*, 263–273. [CrossRef]
35. He, Y.; Yang, T.B.; Ji, Q.; Chen, J.; Shao, W.W. Glacier variation in response to climate change in chinese tianshan mountains from 1989 to 2012. *J. Mt. Sci.* **2015**, *12*, 1189–1202. [CrossRef]
36. Wang, P.; Li, Z.; Huai, B.; Wang, W.; Li, H.; Wang, L. Spatial variability of glacial changes and their effects on water resources in the chinese tianshan mountains during the last five decades. *J. Arid Land* **2015**, *7*, 717–727. [CrossRef]
37. Xu, J.L.; Liu, S.Y.; Guo, W.Q.; Zhang, Z.; Wei, J.F.; Feng, T. Glacial area changes in the ili river catchment (northeastern tian shan) in xinjiang, china, from the 1960s to 2009. *Adv. Meteorol.* **2015**, *2015*, 847257. [CrossRef]

38. Li, Y.-J.; Ding, Y.-J.; Shangguan, D.-H.; Wang, R.-J. Regional differences in global glacier retreat from 1980 to 2015. *Adv. Clim. Change Res.* **2019**, *10*, 203–213. [CrossRef]
39. Li, J.; Xu, X. Glacier change and its response to climate change in western china. *Land* **2023**, *12*, 623. [CrossRef]
40. Wang, Y.; Li, J.; Wu, L.; Guo, L.; Li, J. Using remote sensing images to monitor the glacier changes in qilian mountains during 1987–2018 and analyzing the impact factor. *J. Glaciol. Geocryol.* **2020**, *42*, 344–356.
41. Zhou, Z.; Han, N.; Liu, J.; Yan, Z.; Zhu, J. Glacier variations and their response to climate change in an arid inland river basin of northwest china. *J. Arid Land* **2020**, *12*, 357–373. [CrossRef]
42. Wang, X.; Huang, Y.; Liu, T.; Du, W. Impacts of climate change on glacial retreat during 1990–2021 in the chinese altay mountains. *Catena* **2023**, *228*, 107156. [CrossRef]
43. Narama, C.; Kb, A.; Duishonakunov, M.; Abdrakhmatov, K. Spatial Variability of Recent Glacier Area Changes in the Tien Shan Mountains, Central Asia, Using Corona (~ 1970), Landsat (~ 2000), and Alos (~ 2007) Satellite Data. *Grid Pervasive Comput.* **2010**, *71*, 42–54. [CrossRef]
44. Huang, M.Z.; Ping, Z. An automatic method for clean glacier and nonseasonal snow area change estimation in high mountain asia from 1990 to 2018. *Remote Sens. Environ. Interdiscip. J.* **2021**, *258*, 112376. [CrossRef]
45. Zhuang, L.; Changqing, K.E.; Cai, Y.; Nourani, V. Measuring glacier changes in the tianshan mountains over the past 20 years using google earth engine and machine learning. *J. Geogr. Sci.* **2023**, *33*, 1939–1964. [CrossRef]
46. Wang, L.C.; Yu, K.; Chang, L.; Zhang, J.; Tang, T.; Yin, L.H.; Gu, X.F.; Dong, J.Q.; Li, Y.; Jiang, J. Response of glacier area variation to climate change in the kaidu-kongque river basin, southern tianshan mountains during the last 20 years. *China Geol.* **2021**, *3*, 389–401.
47. Zhang, Q.; Chen, Y.; Li, Z.; Li, Y.; Xiang, Y.; Bian, W. Glacier changes from 1975 to 2016 in the aksu river basin, central tianshan mountains. *J. Geogr. Sci.* **2019**, *29*, 984–1000. [CrossRef]
48. Severskiy, I.; Vilesov, E.; Armstrong, R.; Kokarev, A.; Kogutenko, L.; Usmanova, Z.; Morozova, V.; Raup, B. Changes in glaciation of the balkhash-alakol basin, central asia, over recent decades. *Ann. Glaciol.* **2016**, *57*, 382–394. [CrossRef]
49. Gorelick, N.; Hancher, M.; Dixon, M.; Ilyushchenko, S.; Moore, R. Google earth engine: Planetary-scale geospatial analysis for everyone. *Remote Sens. Environ.* **2017**, *202*, 18–27. [CrossRef]
50. Li, X.; Chen, W.; Cheng, X.; Wang, L. A comparison of machine learning algorithms for mapping of complex surface-mined and agricultural landscapes using ziyuan-3 stereo satellite imagery. *Remote Sens.* **2016**, *8*, 514. [CrossRef]
51. Belgiu, M.; Dragut, L. Random forest in remote sensing: A review of applications and future directions. *ISPRS J. Photogramm.* **2016**, *114*, 24–31. [CrossRef]
52. Congalton, R.G.; Mead, R.A. A quantitative method to test for consistency and correctness in photointerpretation. *Photogramm. Eng. Remote Sens.* **1983**, *49*, 69–74.
53. Myint, S.W.; Gober, P.; Brazel, A.; Grossman-Clarke, S.; Weng, Q. Per-pixels vs object-based classif ication of urban land cover extraction using high spatial resolution imagery. *Remote Sens. Environ.* **2011**, *115*, 1145–1161. [CrossRef]
54. Cao, R.; Chen, Y.; Shen, M.; Chen, J.; Zhou, J.; Wang, C.; Yang, W. A simple method to improve the quality of ndvi time-series data by integrating spatiotemporal information with the savitzky-golay filter. *Remote Sens. Environ. Interdiscip. J.* **2018**, *217*, 244–257. [CrossRef]
55. Jianxin, M.U.; Zhongqin, L.I.; Hui, Z.; Pengbin, L. The global glacierized area: Current situation and recent change, based on the randolph glacier inventory(rgi 6.0) published in 2017. *J. Glaciol. Geocryol.* **2018**, *40*, 238–248.
56. Tang, X.L.; Lv, X.; He, Y. Features of climate change and their effects on glacier snow melting in xinjiang, china—Sciencedirect. *Comptes Rendus Geosci.* **2013**, *345*, 93–100. [CrossRef]
57. Bevington, A.R.; Menounos, B. Accelerated change in the glaciated environments of western canada revealed through trend analysis of optical satellite imagery. *Remote Sens. Environ.* **2022**, *270*, 112862. [CrossRef]
58. Moore, J.C. Glaciology and global climate change. *Engineering* **2018**, *4*, 6–8. [CrossRef]
59. Xianwei, W.; Huijiao, C.; Yaning, C. Topography-related glacier area changes in central tianshan from 1989 to 2015 derived from landsat images and aster gdem data. *Water* **2018**, *10*, 555. [CrossRef]
60. Loibl, D.M.; Lehmkuhl, F. Glaciers and equilibrium line altitudes of the eastern nyainqentanglha range, se tibet. *J. Maps* **2015**, *11*, 575–588. [CrossRef]
61. Sommer, C.; Malz, P.; Seehaus, T.C.; Lippl, S.; Zemp, M.; Braun, M.H. Rapid glacier retreat and downwasting throughout the european alps in the early 21st century. *Nat. Commun.* **2020**, *11*, 3209. [CrossRef]
62. Wang, W.; Xiang, Y.; Gao, Y.; Lu, A.; Yao, T. Rapid expansion of glacial lakes caused by climate and glacier retreat in the central himalayas. *Hydrol. Process.* **2015**, *29*, 859–874. [CrossRef]

Disclaimer/Publisher's Note: The statements, opinions and data contained in all publications are solely those of the individual author(s) and contributor(s) and not of MDPI and/or the editor(s). MDPI and/or the editor(s) disclaim responsibility for any injury to people or property resulting from any ideas, methods, instructions or products referred to in the content.